Nanoscale

Accepted Manuscript

This article can be cited before page numbers have been issued, to do this please use: M. Palabathuni, N. Patil, S. Sen, G. Kumari, S. Guerin and S. Singh, *Nanoscale*, 2026, DOI: 10.1039/D6NR00929H.

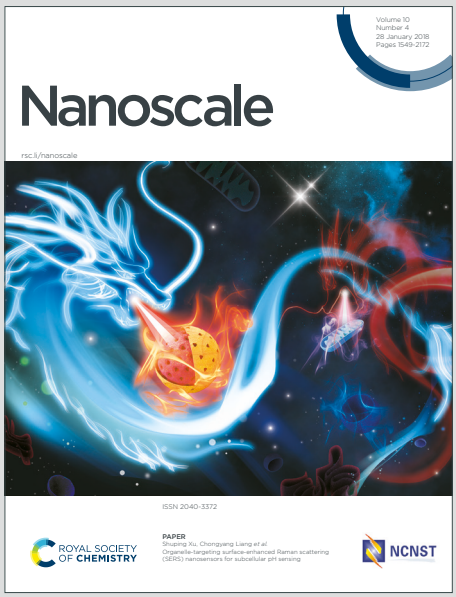

ROYAL SOCIETY OF CHEMISTRY

rsc.li/nanoscale

View Article Online
DOI: 10.1039/D6NR00929H

Influence of Composition-Phase Interplay on Electrochemical Activity of Ternary Transition Metal Dichalcogenides

*Manoj Palabathuni, Niraj Nitish Patil, Suvodeep.Sen, Geetu Kumari, Sarah Guerin, Shalini Singh**

Department of chemical sciences and Bernal institute, University of Limerick, Ireland

Email: shalini.singh@ul.ie

Keywords :- Colloidal synthesis, Ternary nanosheets, Alloying, Phases, Defects

ABSTRACT

Alloying is a powerful strategy to tailor the electronic structures of 2D transition metal dichalcogenides. Controlling the functionalities is essential to explore full potential of these ternary nanosheets with tunable electronic properties. Here, Nb alloyed with W to form ternary $Nb_xW_{1-x}S_2$ nanosheets with different stoichiometric ratios were successfully controlled via colloidal hot-injection synthesis. Incorporation of Nb alters the band structures of parent WS_2, allowing for controlled tunning of electronic properties. High resolution transmission electron microscopy reveals an irregular atomic arrangement at higher Nb concentrations, with a notable transition from pure 2H phase to mixed 2H-1T' phase under controlled concentration of Nb content in the composition. Nb induces a shift of the fermi level, causing transition from semiconducting to metallic nature in ternary nanosheets which allowed for enhanced electrocatalytic activity for the hydrogen evolution reaction (HER) for $Nb_{0.5}W_{0.5}S_2$ compared to pristine WS_2.

View Article Online
DOI: 10.1039/D6NR00929H

INTRODUCTION

Transition metal dichalcogenides (TMDs) are fascinating materials due to their intriguing properties with promising applications in energy conversion and storage.[1,2] In the post graphene era, exploration of atomically thin TMDs has accelerated driven by their layered morphology with remarkable anisotropic physical and electronic properties.[3,4] The rich phase diagram of these layered materials offers distinctive characteristics such as, tunable bandgap, phase dependent conductivity and high carrier mobility.[5–7] In addition, their large surface area, accessible interlayer spacing and unique electronic properties make TMDs particularly attractive for electrocatalytic applications.[8,9]

The electronic properties of TMDs are predominantly determined by their versatile chemical compositions and structural phases. Thus, achieving their full functional potential necessitates deliberate regulation of those electronic properties as a fundamental prerequisite. Unlike most binary TMDs, the tailored ternary counterpart offers additional degree of control for tailoring electronic and surface properties.[10–12] The judicious incorporation of dopants not only expands the structural landscape but also introduces new pathways for electronic modulations.[13] In specific, depending on the choice of metal/chalcogen and their crystal structure, the different localization of atomic d orbitals arising due to the introduction of a third/forth element are crucial in spatial delocalization of their discrete energy levels. At higher dopant concentrations, this effect results in band gap modification and redistribution of the density of states (DOS).[14] Moreover, the intrinsic reduced dimensionality of 2D TMDs further amplifies the effectiveness of such dopant-induced band structure engineering. For instance, bandgap engineering has been well explored in multielement compositions such as $MoS_{2(1-x)}Se_{2x}$, $WS_{2x}Se_{2(1-x)}$, $Mo_{1-x}W_xS_2$, $ReS_{2x}Se_{2(1-x)}$, $Mo_xW_{1-x}S_{2y}Se_{2(1-y)}$, by tuning the chemical composition of metal cations and chalcogen anions.[15–19]

View Article Online
DOI: 10.1039/D6NR00929H

To date, a wide range of metals have been incorporated into WS_2 to tailor its electronic and catalytic properties.[9,20] Early transition metal such as V and Ta can effectively modulate the carrier concentration. However, their incorporation often induces structural instability. In contrast, late transition metals e.g., Fe, Co, Ni tend to form secondary phases rather than true substitutional alloy.[21] In this context, Nb has emerged as one of the effective and widely reported dopant/alloying element for WS_2. Owing to its close atomic size and strong electronic compatibility with W, Nb can be stably incorporated into the WS_2 lattice without disrupting the crystal structure. Also, Nb substitution induces controlled p-type doping and optimizes the local electronic environment, directly regulating charge transfer and hydrogen adsorption energies.[22–24] Despite these advantages, most ternary and quaternary compositions of TMDs, including Nb-substituted WS_2, have been synthesized by using chemical vapour deposition (CVD).[25,26] While CVD enables substitution levels exceeding 10% and has demonstrated a clear n to p-type crossover with metal atoms acted as electron acceptors, the process requires high growth temperatures (>800^{o} C).[27] Such elevated temperatures introduce significant issues in precursor reactivity and volatility, often leading to poor compositional control, inhomogeneous alloying and binary phase separation. These limitations restrict kinetic tunability and hinder the rational design and adoption of these materials in practical applications. Therefore, the design of a general and controllable synthetic strategy remains critical. Compared to high temperature synthesis techniques, colloidal hot injection synthesis route offers a low temperature chemical route that enables precise stoichiometric control and homogenous alloying. This synthetic flexibility enables the tunability of the band structures and systematic modulation of electronic properties.[28,29]

In this study, we report a low-temperature colloidal hot-injection strategy for controlled incorporation of Nb in WS_2 nanosheets enabling the synthesis of ternary $Nb_xW_{1-x}S_2$ over a wide compositional range with precise control of metal stoichiometry. Across all compositions,

View Article Online
DOI: 10.1039/D0NR00929H

the experimentally determined metal ratios closely matched the nominal stoichiometry defined by the starting precursor, conforming reliable compositional control. Structural analysis by high-resolution transmission electron microscopy (HRTEM) reveals the composition dependent crystal phase evolution and defect formations induced by Nb substitution, while X-ray photoelectron spectroscopy (XPS) further evidence corresponding phase transitions. In addition, XPS analysis indicates the formation of sulfur vacancies, and valance band spectra shows that increasing Nb content modifies the electronic structures, leading to band restructuring and a reduced bandgap. These coupled structural and electronic modifications lead to a significant enhancement of electrocatalytic hydrogen evolution reaction (HER) activity in acidic electrolyte of the nanosheets with the mixed phase composition ($x = 0.5$). The improved activity is attributed to the increased density of catalytically active sites arising from sulfur vacancies and enhanced charge transfer enabled by Nb-induced band modulation.

RESULTS & DISCUSSION

$Nb_xW_{1-x}S_2$ nanostructures were synthesised via hot-injection colloidal route using a pre-mixed stock dispersion $W(CO)_6$, $NbCl_5$ and S powder in OLA. The molar ratio of Nb and W precursors in the stock dispersion was adjusted while maintaining the stock volume constant (as given in Table S1, supporting information). This stock was injected into a coordinating ligand/solvent mixture at 300° C and was allowed to react for 120 mins. Here, the precursor selectivity was critical in achieving controlled Nb substitution within the WS_2 lattice. For instance, use of WCl_6 as W source led to formation of oxide by-products and particles enriched in W, Nb ,O and Cl as revealed by XRD and elemental mapping (Figure S1 and 2), even under inert conditions, reflecting on the high oxophilicity of WCl_6.[30] In contrast, $W(CO)_6$ undergoes thermal decomposition to generate metallic W while simultaneously acting as an in situ reducing agent.[31,32] The resulting reductive environment stabilizes lower Nb oxidation states,

View Article Online
DOI: 10.1039/D0NR00929H

thereby facilitating Nb incorporation into WS_2 and promoting ternary phase formation while suppressing Nb oxide impurities in the reaction flask. Moreover, this $W(CO)_6$ based synthesis protocol affords a chemical yield of ~75% (see SI Table S2 for yield calculations), underscoring the efficiency and sustainability of this approach.

The powder X-Ray diffraction (XRD) patterns for all the ternary compositions are shown in Figure 1A. Peaks of $x = 0$, represent the 2H phase WS_2 with lattice constants a = 3.18Å and c = 12.5Å, referenced from the JCPDS: 04-016-3255; $P6_3/mmc$. Highlighted regions show systematic shifts in (002), (100), (110) and (200) peaks with the gradual increase in x. Compositions with a range of x from 0.1 to 0.5 show a linear shift towards lower 2θ angles which signifies the progressive lattice expansion with increasing Nb in the samples. This is further corroborated by the a and c lattice constants (shown in Figure 1 (B and C)) that are derived from the peak positions of (100) and (008). The in-plane lattice parameters (a) expand from 3.16Å ($x = 0$) to 3.29Å ($x = 0.5$) due to larger ionic radius of Nb^{5+} (□0.64 Å) compared to W^{6+} (□0.60 Å).[33] Simultaneously, the out-of-plane parameter (c) contracts from 12.3Å ($x = 0$) to 11.85Å ($x = 0.5$), likely due to the stronger Nb-S bonding and reduced interlayer spacing.[34] However, a deviation from the trend was observed in the samples with $x = 0.7$ and 0.9, which could be attributed to the non-homogeneous mixing of atoms in the lattice. To ensure the phase remains unchanged, XRD of the sample ($x = 0.5$) were recorded before and after annealing at 400°C. There is no change in the peak position and intensities observed, indicating that the crystal structure and phase composition remain intact (Figure S3).

View Article Online
DOI: 10.1039/D6NR00929H

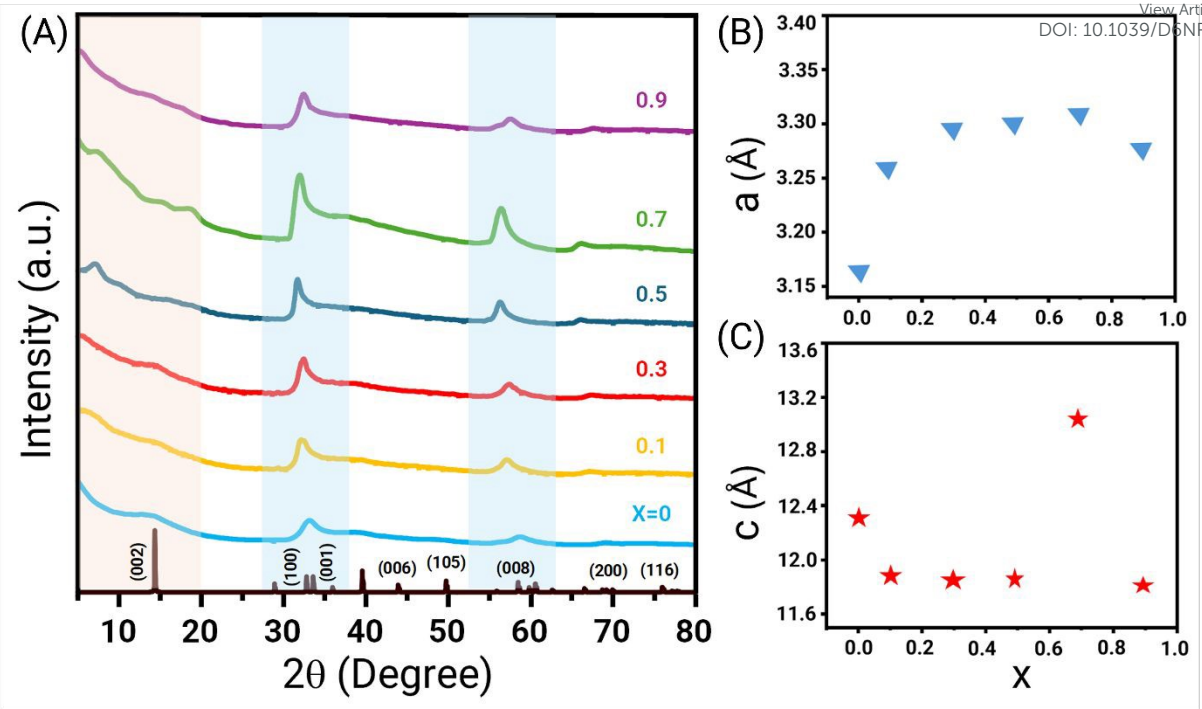

Figure 1. (A) XRD patterns of $W_{1-x}Nb_xS_2$ (x = 0 to 0.9). Shaded regions highlight the shift in diffraction planes. (B) Lattice constant a, (C) Lattice constant c.

Transmission electron microscopy (TEM) images of $Nb_xW_{1-x}S_2$ (x = 0, 0.1, 0.3 and 0.7) with insets of histogram, are shown in Figure 2a. The side view (of sample, x = 0.5) high-resolution TEM image confirms abundant exposed edges shown in Figure 2b with an interlayer spacing of 0.7 nm (Figure S4). The elemental mapping was obtained using Energy-Dispersive X-Ray Spectroscopy (EDS) for x = 0.5 sample (Figure 2c), confirming the homogenous distribution of W, Nb and S. The results of the remaining samples (x = 0.1, 0.3, 0.7) given in Figure S5. The stochiometric ratios of elements in all samples were confirmed by X-ray photoelectron spectroscopy (XPS) and inductively coupled plasma atomic emission spectroscopy (ICP-OES) (Table S1). The data indicate that the atomic ratios of metals were almost same as those of the precursors $[W(CO)_6]$:$[NbCl_5]$ reflecting positively on the chemical yield of the synthetic approach. The ratio of [S]/[W]+[Nb] is close to 2 for samples till the content of $x \leq 0.7$, suggesting that the S vacancies are negligible. Whereas, this ratio decreases at higher x values,

View Article Online
DOI: 10.1039/D5NR00929H

indicating sulfur vacancy formation at higher Nb content, evident from the XPS and SEM-EDS spectra (in supporting Figure S6-8)

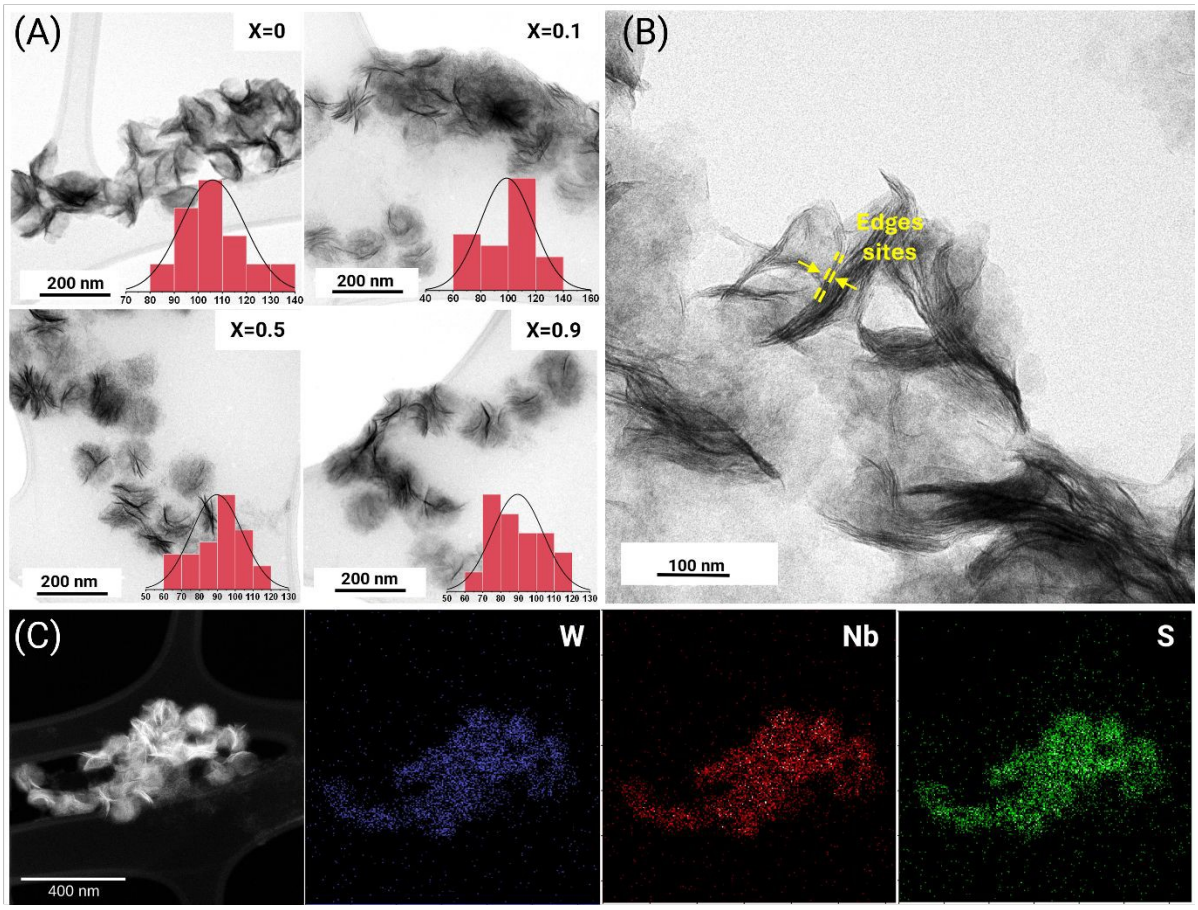

Figure 2. (A) TEM images of $W_{1-x}Nb_xS_2$ (x = 0, 0.1, 0.5 and 0.9) each with an inset histogram, showing the corresponding nanosheets distribution and average size. (B) Enlarged TEM image of x = 0.5. (C) STEM (x = 0.5), elemental mapping showing the spatial distribution of W, Nb and S, confirming the uniform elemental dispersion across the nanosheets.

View Article Online
DOI: 10.1039/D6NR00929H

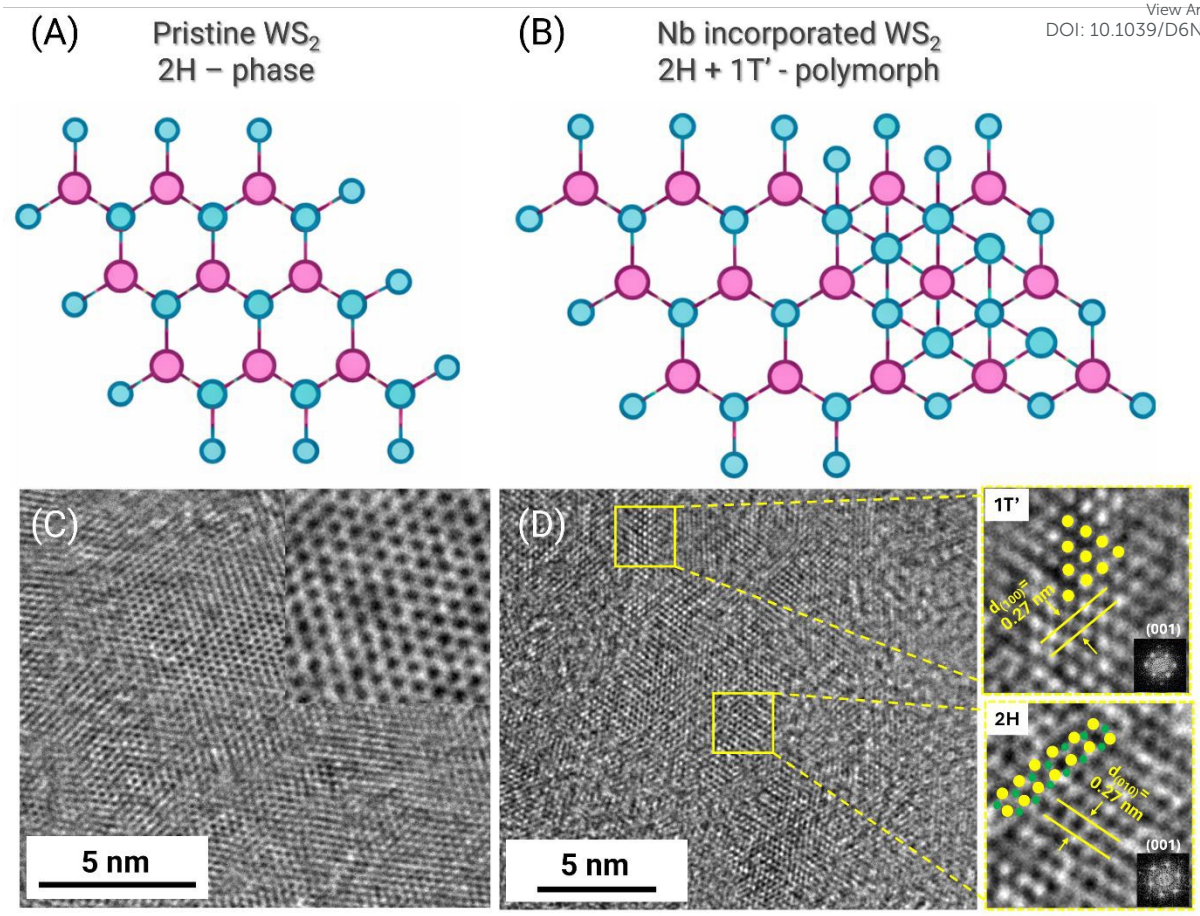

Figure 3. Ball-and-stick models illustrates the crystal structures of (A) 2H and (B) 2H-1T' phase. HRTEM image of $Nb_xW_{1-x}S_2$ NSs (C) at $x = 0$, with an enlarged inset, (D) $x = 0.1$, where yellow highlight indicates (2H) and (1T') regions. Enlarged view of the highlighted areas are shown on the right side. The 2H and 1T' atomic arrangement shown in yellow and green dots.

HRTEM analysis of $Nb_xW_{1-x}S_2$ nanosheets was performed to investigate the structural impact of Nb substitution. Interestingly, the analysis revealed phase transition in the ternary composition. Figure 3a and b provides an overview of 2H and 1T' crystal structures, which are known polymorphs of WS_2. The 2H phase exhibits a trigonal prismatic coordination with hexagonal symmetry, while the 1T' phase shows a distorted octahedral coordination with metallic behaviour. The HRTEM image of WS_2 shows the arrangement of W and S in a hexagonal ring pattern matched with the overlaid ball-and-stick model of H-phase WS_2

View Article Online
DOI: 10.1039/D0NR00929H

Nanosheets (x = 0), shown in Figure 3c consistent with the hexagonal symmetry of the 2H phase, including an interplanar spacing ($d_{(100)}$ = 0.27 nm).

When $x \geq 0.1$, the coexistence of both 2H and 1T' phases are observed, as shown in Figure 3d, indicating that Nb alloying induces the partial phase transition. The highlighted yellow region is 2H and 1T' phases with an enlarged HRTEM on the left. The observed interplanar spacing of 0.27 nm for (010) plane in 2H and the (100) plane in 1T' supports the presence of mixed phase domains resulting from substitution of Nb at x = 0. Beyond $x > 0.1$, we observed severe lattice irregularities, with disrupted fringes and unclear periodicity in several regions as shown in Figure S9. Thus, it confirms that, at higher concentrations of x destabilizes the pristine 2H lattice, promoting mixed phase and defect formation with in the nanosheets. However, such irregularities are commonly associated with electrocatalytic activity, as they serve as active sites for electrocatalysis.

XPS analysis of $Nb_xW_{1-x}S_2$ shown in Figure 4, revealed the distinct shift in binding energies, indicating the changes in electronic properties due to Nb incorporation. The deconvoluted spectra of W 4f and Nb 3d confirms the presence of different oxidation states, suggesting charge distribution when x>0. Clear sign of composition tunning is shown in the survey scan (Figure 4a), W 4f peak intensity decreases with increasing x, while the Nb 3d peak intensity increases. Valance band spectroscopy (VBS) of all the composition reveals the valance band maximum (VBM) Fermi energy level (E_F) as shown in Figure 4b. The VBM appeared for pristine WS_2 ($\geq$0 eV) and (<0 eV) for all the ternary compositions. As the Nb increases, the downshift of the metal d-states relative to the Fermi level, suggesting a decrease in the d-band center (ε_d).[35] This indicates, Nb content induces a semiconductor to metallic behaviour transition. which is further supported by the W4f spectra analysis as discussed below.

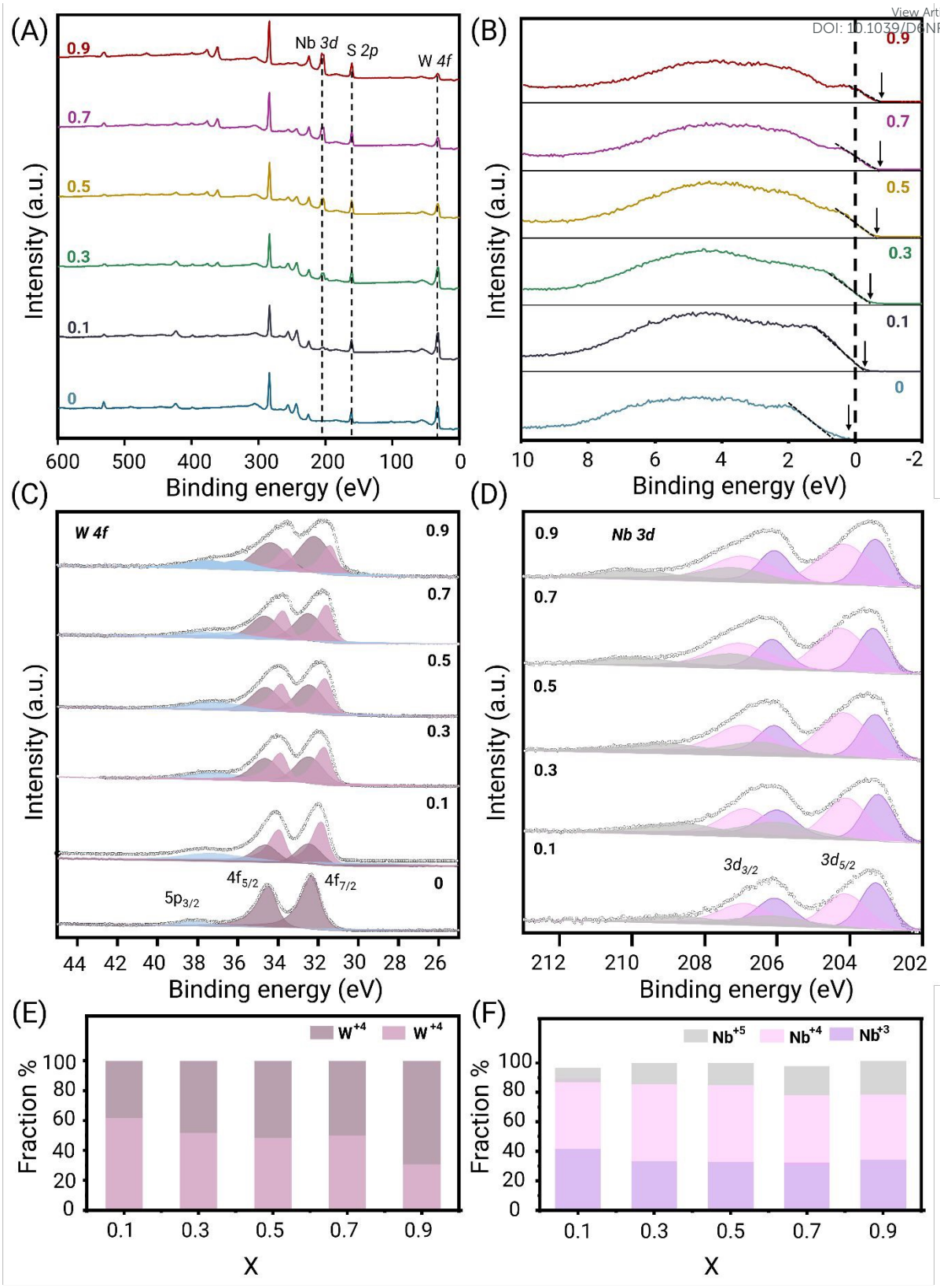

Figure 4. (A) XPS survey scan of $Nb_xW_{1-x}S_2$ confirming the presence of W, Nb and S. (B) VBS of $x \geq 0$. High-resolution XPS peaks of (C) W - $4f_{7/2}$ and $4f_{5/2}$, (D) Nb – $3d_{5/2}$ and $3d_{3/2}$. Fraction

View Article Online
DOI: 10.1039/D0NR00929H

percentage of (E) Nb and (F) W oxidation states vs *x* obtained by deconvolution of Nb 3d and W4f peaks respectively.

Two characteristics peaks of W were observed (Figure 4c) - W $4f_{7/2}$ at 32.3 eV and $4f_{5/2}$ at 34.5 eV. In WS_2, the $4f_{7/2}$ peak at 32.3 eV (blueshift from neutral W at 31.2 eV) attributed to the naturally occurring semiconductive 2H phase (W-S binding structures). However, the deconvolution of $x \geq 0.1$ composition possesses two additional peaks at 31.8 eV and 33.9 eV, corresponding to 1T' phase, as already discussed above section during HRTEM analysis.[36] The extra electrons introduced by Nb destabilize the pure semiconducting structure and initiate a 2H → 1T' phase transition. The new peaks of 1T' phase shown decrease in binding energies as Nb concentration increases. This could be observed owing to the shift in fermi levels caused by increased density of d-orbital electrons. Similarly, the deconvolution of the Nb $3d_{5/2}$ peak shown in Figure 4d identifies Nb^{3+}, Nb^{4+}, and Nb^{5+} states at 203.3, 204.1, and 206.1 eV respectively.

The variations in oxidation states of W and Nb (as shown in Figure e and f), deconvoluted from the W $4f_{7/2}$ and Nb $3d_{5/2}$ peaks across all the composition. Despite phase coexistence W remains entirely consistent in the +4 oxidation states. Whereas, Nb identified in Nb^{3+}, Nb^{4+} and Nb^{5+} ion states. The Nb^{5+} states originated from the Nb-O bonding structures, the fraction of the Nb^{5+} states rises, suggesting electron depletion by W ions along with increased surface oxidation.[37] whereas the Nb^{3+} and Nb^{4+} states originated from the Nb-S bonding structure. The reducing environment created from the decomposition of $W(CO)_6$ helps to stabilize these lower oxidation states, while restricting fully formation Nb oxide species at Nb^{5+} states.

View Article Online
DOI: 10.1039/D6NR00929H

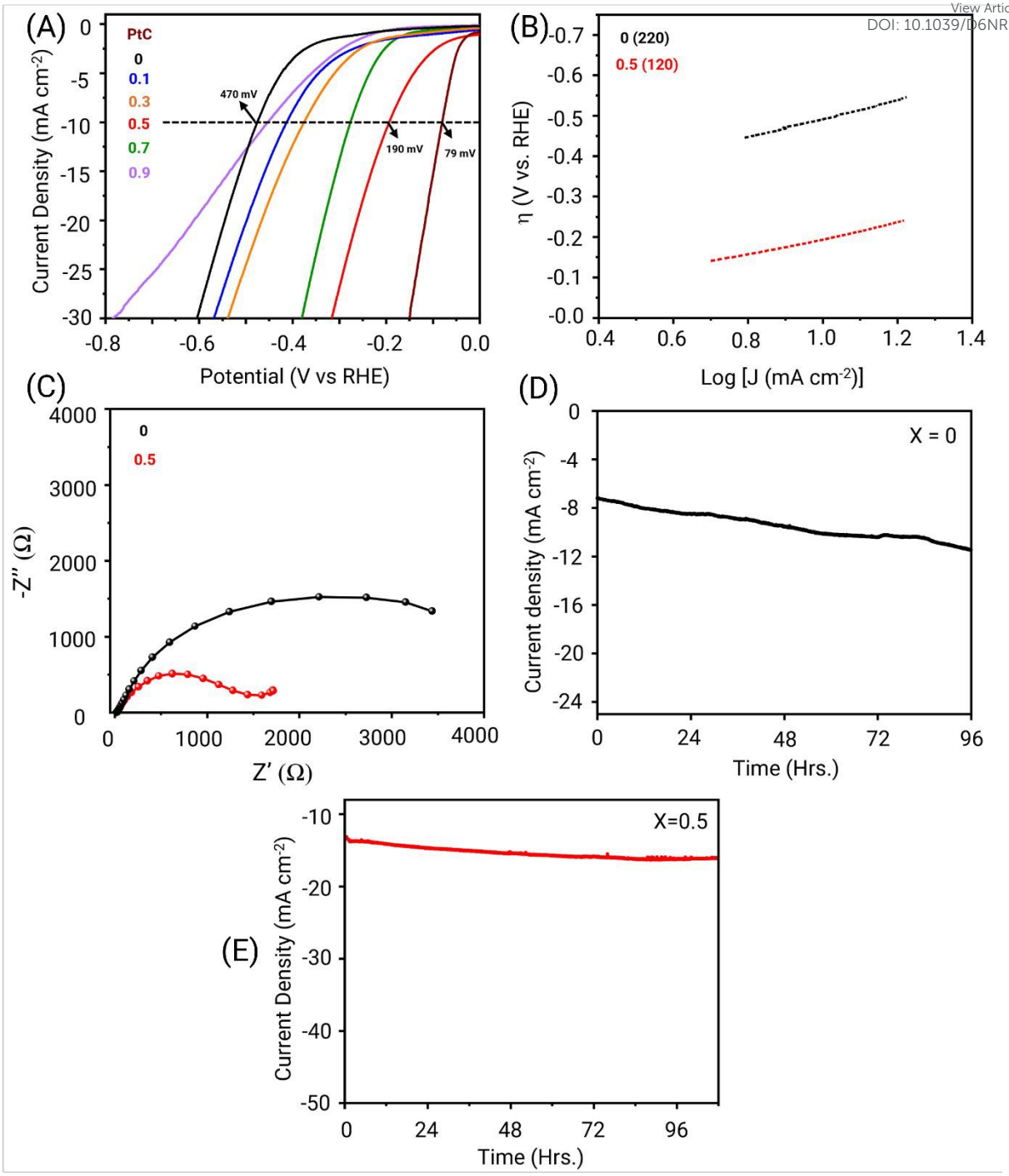

Figure 5. HER performance of $Nb_xW_{1-x}S_2$ ternary nanosheets (current density and overpotential at 10 mA cm^{-2}), (A) Polarization curves with scan rate of 2 mV s^{-1}, (B) corresponding slopes, (C) Nyquist plot from Electrochemical Impedance Spectroscopy (EIS). Chronoamperometric stability of samples: (D) $x = 0$ at –0.470 V and (E) $x = 0.5$ at – 0.190 V.

View Article Online
DOI: 10.1039/D6NR00929H

Electrocatalytic HER reaction

Electrocatalytic HER performance of $Nb_xW_{1-x}S_2$ was evaluated in the acidic electrolyte (0.5 M H_2SO_4). Figure 5a depicts the linear sweep voltammetry (LSV) using the applied potentials *vs* reversible hydrogen electrode (RHE), which is equal to the overpotentials (η). $\eta_{J=10}$ denotes the η value at $J = 10$ mA cm^{-2}. The $x = 0.5$ composition exhibits the lowest overpotentials values such as 190 mV, among all the ternary compositions. The low potential region was converted to the Tafel slope shown in figure 5b was obtained using the linear fitting, its value is 120 mV dec^{-1} at ($x = 0.5$). In comparison, the commercial 20 wt% Pt/C catalyst as a reference sample exhibited $\eta_{J=10} = 79$ mV.

Figure 5a illustrates the composition dependence of the HER performance, maximum performance was observed for $x = 0.5$ sample. This composition activity is superior to the previously reported across various modified TMDs systems including doping, alloying, heterostructures are provided in Table S3. In support to the LSV data, the EIS data in Figure 5c demonstrated a comparable composition-dependent behaviour, highlighting the pivotal role of charge transfer resistance (R_{CT}) in determining performance. The fitted charge-transfer resistance (R_{CT}) for the sample exhibiting the best HER performance ($x = 0.5$) is 157 Ω, whereas it is 1530 Ω for WS_2. The results indicate that transfer kinetics are significantly improved in ($x = 0.5$) sample. Long-term chronoamperometry (Figure 5d and e) shows that, unlike the $x = 0$, sample, the $x = 0.5$ sample maintained stable current for nearly 100hr.

Substituting Nb, induces a semiconductor to semi metallic transition, as confirmed by the shift of the valance band maximum in the XPS. We observed increased HER performance at $x = 0.5$, highlighting the importance of optimizing Nb for improved HER activity. At ($x = 0.5$), the Nb concentration likely enhanced the electrical conductivity confirmed from the EIS analysis and simultaneously increases the HER active sites. However, higher concentrations of Nb

View Article Online
DOI: 10.1039/D0NR00929H

content deteriorate the performance. This can be due to excessive structural distortion or defects formations that hinders electron transfer, increasing the overpotentials and slowing down the reaction kinetics. On the other hand, with increasing *x*, the formation of oxide species becomes more pronounced (evidence from XPS data supports the observation), which negatively impact the electrocatalytic performance by increasing the charge transfer resistance and reducing the availability of H^+ absorption sites. The results demonstrate that a carefully optimized ternary composition is crucial for achieving the best HER performance in acidic media, as balance between conductivity, structural distortions and active sites governs the overall catalytic efficiency.

CONCLUSION

In summary, we successfully synthesized ternary alloy nanosheets via colloidal hot injection technique demonstrating the critical role of precursor selectivity. Fully tunable control on composition was achieved, enabling systematic modulation of their structural and electronic properties. Confirmed uniform nanosheet morphology with accurate Nb stoichiometries using XPS, ICP, and SEM-EDX. The TEM revealed the transition from pure 2H to coexistence of 2H and 1T' at $x = 0.1$, further increased concentration ($x \geq 0.3$) induced more defect formation and irregular arrangement in the lattice. The oxidation became more significant at higher *x*, which hinders the catalytic activity, alloy nanosheets at $x = 0.5$ shown the exceptional HER activity with a $\eta = 190$ mV (at $J = 10$ mA cm^{-2}) and demonstrates a remarkable stability over 100hr at -0.2 V. In support, XPS-derived VBM indicate band restructuring and fermi level shifts, collectively contributes to exceptional HER activity. Our study highlights how stoichiometric engineering can effectively tailor the structural and electronic properties of 2D TMDs. These understanding provide a rational designing next generation earth abundant electrocatalysts for sustainable energy conversions.

View Article Online
DOI: 10.1039/D6NR00929H

Note

The authors declare no competing financial interest.

Acknowledgments

This publication has emanated from research conducted with the financial support of Taighde Éireann - Research Ireland under Grant number 22/FFP-P/11591. M.P. acknowledge IRC (GOIPG/2024/3075) for funding. N.N.P. acknowledges funding from AMBER (12/rc/2278_p2). S.S. acknowledges Horizon TMA MSCA Postdoctoral Fellowship (Project ID 101207456).

REFERENCES

(1) Gupta, S.; Zhang, J.-J.; Lei, J.; Yu, H.; Liu, M.; Zou, X.; Yakobson, B. I. Two-Dimensional Transition Metal Dichalcogenides: A Theory and Simulation Perspective. *Chem. Rev.* **2025**, *125* (2), 786–834. https://doi.org/10.1021/acs.chemrev.4c00628.

(2) Roy, S.; Joseph, A.; Zhang, X.; Bhattacharyya, S.; Puthirath, A. B.; Biswas, A.; Tiwary, C. S.; Vajtai, R.; Ajayan, P. M. Engineered Two-Dimensional Transition Metal Dichalcogenides for Energy Conversion and Storage. *Chem. Rev.* **2024**, *124* (16), 9376–9456. https://doi.org/10.1021/acs.chemrev.3c00937.

(3) Gupta, A.; Sakthivel, T.; Seal, S. Recent Development in 2D Materials beyond Graphene. *Prog. Mater. Sci.* **2015**, *73*, 44–126. https://doi.org/10.1016/j.pmatsci.2015.02.002.

(4) Manzeli, S.; Ovchinnikov, D.; Pasquier, D.; Yazyev, O. V.; Kis, A. 2D Transition Metal Dichalcogenides. *Nat. Rev. Mater.* **2017**, *2* (8), 17033. https://doi.org/10.1038/natrevmats.2017.33.

(5) *Bandgap engineering of two-dimensional semiconductor materials | npj 2D Materials and Applications*. https://www.nature.com/articles/s41699-020-00162-4 (accessed 2026-02-23).

(6) Fu, Q.; Han, J.; Wang, X.; Xu, P.; Yao, T.; Zhong, J.; Zhong, W.; Liu, S.; Gao, T.; Zhang, Z.; Xu, L.; Song, B. 2D Transition Metal Dichalcogenides: Design, Modulation, and Challenges in Electrocatalysis. *Adv. Mater.* **2021**, *33* (6), 1907818. https://doi.org/10.1002/adma.201907818.

(7) Chia, X.; Pumera, M. Characteristics and Performance of Two-Dimensional Materials for Electrocatalysis. *Nat. Catal.* **2018**, *1* (12), 909–921. https://doi.org/10.1038/s41929-018-0181-7.

(8) Kapuria, N.; Patil, N. N.; Ryan, K. M.; Singh, S. Two-Dimensional Copper Based Colloidal Nanocrystals: Synthesis and Applications. *Nanoscale* **2022**, *14* (8), 2885–2914. https://doi.org/10.1039/D1NR06990J.

(9) Zhou, P.; Schiettecatte, P.; Vandichel, M.; Rousaki, A.; Vandenabeele, P.; Hens, Z.; Singh, S. Synthesis of Colloidal WSe2 Nanocrystals: Polymorphism Control by Precursor-Ligand Chemistry. *Cryst. Growth Des.* **2021**, *21* (3), 1451–1460. https://doi.org/10.1021/acs.cgd.0c01036.

(10) Pham, X.-M.; Patil, N. N.; Ahad, S. A.; Kapuria, N.; Owusu, K. A.; Geaney, H.; Singh, S.; Ryan, K. M. Electrophoretic Assisted Fabrication of Additive-Free WS2 Nanosheet Anodes for High Energy Density Lithium-Ion Batteries. *Nanoscale* **2024**, *16* (44), 20496–20504. https://doi.org/10.1039/D4NR03025G.

(11) Mastrippolito, D.; Shahmanesh, A.; Cavallo, M.; Bossavit, E.; Abed, I. L. E.; Dabard, C.; Singh, S.; Silly, M. G.; Capitani, F.; Peric, N.; Biadala, L.; Zitolo, A.; Avila, J.; Carlà, F.; Tresca, C.; Lhuillier, E.; Mahler, B.; Pierucci, D. In Situ Investigation of 1T′/1H Phase Transition in Colloidal WS2 Monolayers. *Nanoscale* **2025**, *17* (43), 25174–25186. https://doi.org/10.1039/D5NR03092G.

(12) Zhang, H. Ultrathin Two-Dimensional Nanomaterials. *ACS Nano* **2015**, *9* (10), 9451–9469. https://doi.org/10.1021/acsnano.5b05040.

(13) Muller, S. E.; Prange, M. P.; Lu, Z.; Rosenthal, W. S.; Bilbrey, J. A. An Open Database of Computed Bulk Ternary Transition Metal Dichalcogenides. *Sci. Data* **2023**, *10* (1), 336. https://doi.org/10.1038/s41597-023-02103-4.

(14) Kim, J. H.; Sung, H.; Lee, G.-H. Phase Engineering of Two-Dimensional Transition Metal Dichalcogenides. *Small Sci.* **2024**, *4* (1), 2300093. https://doi.org/10.1002/smsc.202300093.

(15) Cui, F.; Feng, Q.; Hong, J.; Wang, R.; Bai, Y.; Li, X.; Liu, D.; Zhou, Y.; Liang, X.; He, X.; Zhang, Z.; Liu, S.; Lei, Z.; Liu, Z.; Zhai, T.; Xu, H. Synthesis of Large-Size 1T′ ReS2xSe2(1−x) Alloy Monolayer with Tunable Bandgap and Carrier Type. *Adv. Mater.* **2017**, *29* (46), 1705015. https://doi.org/10.1002/adma.201705015.

(16) Kang, H. S.; Kang, J. H.; Lee, S.; Lee, K.; Koo, D. H.; Kim, Y.-S.; Hong, Y. J.; Kim, Y.-J.; Kim, K.; Lee, D.; Lee, C.-H. Bowing-Alleviated Continuous Bandgap Engineering of Wafer-Scale WS2xSe2(1-x) Monolayer Alloys and Their Assembly into Hetero-Multilayers. *NPG Asia Mater.* **2022**, *14* (1), 90. https://doi.org/10.1038/s41427-022-00437-w.

(17) Susarla, S.; Kutana, A.; Hachtel, J. A.; Kochat, V.; Apte, A.; Vajtai, R.; Idrobo, J. C.; Yakobson, B. I.; Tiwary, C. S.; Ajayan, P. M. Quaternary 2D Transition Metal

View Article Online
DOI: 10.1039/D6NR00929H

Dichalcogenides (TMDs) with Tunable Bandgap. *Adv. Mater.* **2017**, *29* (35). https://doi.org/10.1002/adma.201702457.

(18) Feng, Q.; Mao, N.; Wu, J.; Xu, H.; Wang, C.; Zhang, J.; Xie, L. Growth of MoS2(1−x)Se2x (x = 0.41–1.00) Monolayer Alloys with Controlled Morphology by Physical Vapor Deposition. *ACS Nano* **2015**, *9* (7), 7450–7455. https://doi.org/10.1021/acsnano.5b02506.

(19) Wang, Z.; Liu, P.; Ito, Y.; Ning, S.; Tan, Y.; Fujita, T.; Hirata, A.; Chen, M. Chemical Vapor Deposition of Monolayer Mo1−xWxS2 Crystals with Tunable Band Gaps. *Sci. Rep.* **2016**, *6* (1), 21536. https://doi.org/10.1038/srep21536.

(20) Jaramillo, T. F.; Jørgensen, K. P.; Bonde, J.; Nielsen, J. H.; Horch, S.; Chorkendorff, I. Identification of Active Edge Sites for Electrochemical H2 Evolution from MoS2 Nanocatalysts. *Science* **2007**, *317* (5834), 100–102. https://doi.org/10.1126/science.1141483.

(21) Yang, Y.; Fan, X.-L.; Pan, R.; Guo, W.-J. First-Principles Investigations of Transition-Metal Doped Bilayer WS2. *Phys. Chem. Chem. Phys.* **2016**, *18* (15), 10152–10157. https://doi.org/10.1039/C6CP00701E.

(22) Wu, X.; Zhang, H.; Zhang, J.; Lou, X. W. (David). Recent Advances on Transition Metal Dichalcogenides for Electrochemical Energy Conversion. *Adv. Mater.* **2021**, *33* (38), 2008376. https://doi.org/10.1002/adma.202008376.

(23) Chia, X.; Eng, A. Y. S.; Ambrosi, A.; Tan, S. M.; Pumera, M. Electrochemistry of Nanostructured Layered Transition-Metal Dichalcogenides. *Chem. Rev.* **2015**, *115* (21), 11941–11966. https://doi.org/10.1021/acs.chemrev.5b00287.

(24) Tan, S. M.; Sofer, Z.; Luxa, J.; Pumera, M. Aromatic-Exfoliated Transition Metal Dichalcogenides: Implications for Inherent Electrochemistry and Hydrogen Evolution. *ACS Catal.* **2016**, *6* (7), 4594–4607. https://doi.org/10.1021/acscatal.6b00761.

(25) Feng, L.; Jiang, W.; Su, J.; Zhou, L.; Liu, Z. Performance of Field-Effect Transistors Based on NbxW1−xS2 Monolayers. *Nanoscale* **2016**, *8* (12), 6507–6513. https://doi.org/10.1039/C6NR00380J.

(26) Qin, Z.; Loh, L.; Wang, J.; Xu, X.; Zhang, Q.; Haas, B.; Alvarez, C.; Okuno, H.; Yong, J. Z.; Schultz, T.; Koch, N.; Dan, J.; Pennycook, S. J.; Zeng, D.; Bosman, M.; Eda, G. Growth of Nb-Doped Monolayer WS2 by Liquid-Phase Precursor Mixing. *ACS Nano* **2019**, *13* (9), 10768–10775. https://doi.org/10.1021/acsnano.9b05574.

(27) Tang, L.; Tan, J.; Nong, H.; Liu, B.; Cheng, H.-M. Chemical Vapor Deposition Growth of Two-Dimensional Compound Materials: Controllability, Material Quality, and Growth Mechanism. *Acc. Mater. Res.* **2021**, *2* (1), 36–47. https://doi.org/10.1021/accountsmr.0c00063.

(28) Chhowalla, M.; Shin, H. S.; Eda, G.; Li, L.-J.; Loh, K. P.; Zhang, H. The Chemistry of Two-Dimensional Layered Transition Metal Dichalcogenide Nanosheets. *Nat. Chem.* **2013**, *5* (4), 263–275. https://doi.org/10.1038/nchem.1589.

(29) Jin, H.; Guo, C.; Liu, X.; Liu, J.; Vasileff, A.; Jiao, Y.; Zheng, Y.; Qiao, S.-Z. Emerging Two-Dimensional Nanomaterials for Electrocatalysis. *Chem. Rev.* **2018**, *118* (13), 6337–6408. https://doi.org/10.1021/acs.chemrev.7b00689.

(30) Bianchi, S.; Bortoluzzi, M.; Castelvetro, V.; Marchetti, F.; Pampaloni, G.; Pinzino, C.; Zacchini, S. The Reactivity of Tungsten Hexachloride with Tetrahydrofuran and 2-Methoxyethanol. *Polyhedron* **2016**, *117*, 769–776. https://doi.org/10.1016/j.poly.2016.07.024.

(31) He, R.; Lee, S.; Ding, Y.; Huang, C.; Lu, X.; Zheng, L.; Yu, A.; Zhang, C.; Li, C.; Bi, X.; Li, Y.; Liao, Y.; Li, J.; Ostovari Moghaddam, A.; Yernar, S.; Xu, Y.; Ibáñez, M.; Zhang, C.; Yang, L.; Zhou, Y.; Cabot, A. Amorphous High Entropy Alloy Nanosheets Enabling Robust Li–S Batteries. *Adv. Funct. Mater.* **2026**, *36* (5), e13859. https://doi.org/10.1002/adfm.202513859.

(32) Zhao, X.; Di, Q.; Li, M.; Yang, Q.; Zhang, Z.; Guo, X.; Fan, X.; Deng, K.; Chen, W.; Zhang, J.; Fang, J.; Quan, Z. Generalized Synthesis of Uniform Metal Nanoparticles Assisted with Tungsten Hexacarbonyl. *Chem. Mater.* **2019**, *31* (12), 4325–4329. https://doi.org/10.1021/acs.chemmater.9b00219.

(33) Shannon, R. D. Revised Effective Ionic Radii and Systematic Studies of Interatomic Distances in Halides and Chalcogenides. *Acta Crystallogr. A* **1976**, *32* (5), 751–767. https://doi.org/10.1107/S0567739476001551.

(34) Fan, K.; Shi, M.; Li, H.; Xiang, Z.; Chen, X. Two-Dimensional Superconductivity in New Niobium Dichalcogenides-Based Bulk Superlattices. *Phys. Rev. Mater.* **2025**, *9* (3), 034804. https://doi.org/10.1103/PhysRevMaterials.9.034804.

(35) Chen, W.; Qian, G.; Wang, H.; Chen, D.; Zhou, X.; Yuan, W.; Duan, X. Rationalizing the D-Band Model from Theory to Practice in Catalyst Design. *J. Am. Chem. Soc.* **2025**, *147* (51), 46729–46744. https://doi.org/10.1021/jacs.5c17673.

(36) Kapuria, N.; Patil, N. N.; Sankaran, A.; Laffir, F.; Geaney, H.; Magner, E.; Scanlon, M.; Ryan, K. M.; Singh, S. Engineering Polymorphs in Colloidal Metal Dichalcogenides: Precursor-Mediated Phase Control, Molecular Insights into Crystallisation Kinetics and Promising Electrochemical Activity. *J. Mater. Chem. A* **2023**, *11* (21), 11341–11353. https://doi.org/10.1039/D2TA09892J.

(37) Ma, Q.; Rosenberg, R. A. Angle-Resolved X-Ray Photoelectron Spectroscopy Study of the Oxides on Nb Surfaces for Superconducting r.f. Cavity Applications. *Appl. Surf. Sci.* **2003**, *206* (1), 209–217. https://doi.org/10.1016/S0169-4332(02)01238-2.

View Article Online
DOI: 10.1039/D6NR00929H

Data Availability Statement

The data that support the findings of this study are available on request from the corresponding author.

Supplementary information includes material and method for synthesis of nanostructures with extra data regarding: (i) XRD analysis, (ii) ICP-OES data (iii) STEM-EDX data (iv) SEM – EDS spectrums for stoichiometric ratios (v) HRTEM – for lattice distortions or defect formation (vi) XPS spectra.